Phase diagrams and crystal-fluid surface tensions in additive and nonadditive two-dimensional binary hard-disk mixtures

Shang-Chun Lin* and Martin Oettel†
Institut für Angewandte Physik, Universität Tübingen, Auf der Morgenstelle 10, 72076 Tübingen, Germany

(Received 16 May 2018; published 23 July 2018)

Using density functionals from fundamental measure theory, phase diagrams and crystal-fluid surface tensions in additive and nonadditive (Asakura-Oosawa model) two-dimensional binary hard-disk mixtures are determined for the whole range of size ratios q = small diameter/large diameter, assuming random disorder (lattice points or interstitial occupied by large or small disks at random) in the crystal phase. The fluid-crystal transitions are first order due to the assumption of a periodic unit cell in the density-functional calculations. Qualitatively, the shape of the phase diagrams is similar to the case of three-dimensional hard-sphere mixtures. For the nonadditive case, a broadening of the fluid-crystal coexistence region is found for small q, whereas for large q a vapor-fluid transition intervenes. In the additive case, we find a sequence of spindle-type, azeotropic, and eutectic phase diagrams upon lowering q from 1 to 0.6. The transition from azeotropic to eutectic is different from the three-dimensional case. Surface tensions in general become smaller (up to a factor 2) upon addition of a second species and they are rather small. The minimization of the functionals proceeds without restrictions and optimized graphics card routines are used.

DOI: 10.1103/PhysRevE.98.012608

I. INTRODUCTION

The fluid-crystal transition in two-dimensional (2D) systems of hard disks has been of fundamental interest over the past years. Only recently, it has been established in the one-component system by simulations [1] and experiments [2] that the transition happens via a first-order transition from the fluid to the hexatic phase and a continuous transition from the hexatic to the crystal phase. Although the crystal phase is not strictly periodic (it does not have infinitely long-range positional order), in simulations and experiments it has practically the appearance of a conventional periodic crystal. Therefore, 2D hard disks have a similar status as a model system for crystallization in films and monolayers as 3D hard spheres have for crystallization in the bulk. Besides simulations, classical density-functional theory (DFT) for hard-particle systems has reached a certain maturity and accuracy owing to the development of fundamental measure theory, starting with the work of Rosenfeld [3]. For 2D hard disks, a functional has been proposed in Ref. [4] which gives a very accurate description of fluid structure in one- and two-component systems [5], as well as values for the fluid and crystal coexistence densities which are rather close to the ones of the first-order fluid-hexatic transition [4]. In these fundamental measure theory (FMT) calculations, strict periodicity of the crystal phase was assumed.

Crystals in binary hard-disk systems have been studied some time ago by older density-functional methods in Refs. [6,7] (variants of weighted-density functionals with restricted minimizations). For substitutionally disordered crystals, a sequence of phase diagram types (spindle, azeotropic, and eutectic) has been found upon lowering the disk size ratio similar to the case of 3D hard spheres [8], although the exact shape and the transition size ratios differ considerably between Refs. [6,7]. In these cases, the crystals were assumed strictly periodic as well. In Ref. [9], a survey of possible alloy phases was undertaken in a special zero-temperature limit (identifying the highest-packing-fraction structure among all candidates).

In past decade, phase field crystal (PFC) models have emerged as an efficient tool to phenomenologically describe phase diagrams of binary systems in two and three dimensions [10,11] and of the crystal-fluid surface tension [12]. The PFC models employ a certain Taylor expansion of direct correlation functions among species to produce the desired crystal structure and use several parameters to capture material properties. Whereas the approach is suited to describe the mesoscale behavior of solidification generically, a link to the density distributions in specific crystals is difficult to establish. An example is the hard-sphere system where the PFC fails to describe quantitatively vacancy concentrations, surface tensions, and associated density profiles [13].

Only recently, a binary mixture with a fixed-size ratio of 1/1.4 was investigated by simulations aiming at the fate of the hexatic phase [14] in disordered crystals. The hexatic phase was found to disappear quickly upon addition of the smaller species; overall, a phase diagram of eutectic type was found for this size ratio.

Here we employ the FMT functional of Ref. [4] to study phase diagrams and crystal-fluid surface tensions for additive and nonadditive binary hard-disk mixtures. The nonadditive case is the 2D variant [15] of the well-known Asakura-Oosawa (AO) model [16,17], originally formulated for a mixture of 3D hard spheres where there are no interactions between particles of the second component (depletant). The depletants lead to an effective attractive potential between particles of the first

*shang-chun-lin@uni-tuebingen.de
†martin.oettel@uni-tuebingen.de

species (which for small-size ratios is strictly a two-body potential), therefore the study of the AO model is equivalent to a study of hard disks with additional short-range attractions. The derivation of the AO functional from the functional of Ref. [4] proceeds by employing the linearization trick already studied in the 3D case [18,19]. We examine the case of random disorder (lattice points or interstitials occupied by large or small disks at random) crystal over the whole range of possible size ratios. Random disorder includes the cases of substitutional disorder when disk sizes are comparable, interstitial disorder for small-size ratios, and superpositions of alloy configurations for intermediate-size ratios.

The paper is organized as follows. In Sec. II we introduce the theoretical background for the AO model, FMT, and the FMT-based AO functional. In Sec. III we discuss the numerical treatment of the full minimization of the functionals for bulk crystals and crystal-fluid surfaces. In Sec. IV we present our results for density distributions in the crystal and crystal-fluid interfaces, for phase diagrams, and for surface tensions. In Sec. V we summarize and discuss our results.

II. THEORY

A. Hard-disk mixture and the Asakura-Oosawa model

We consider a mixture of large (l) and small (s) disks, with diameters σ_l and σ_s, respectively, and $q = \frac{\sigma_\mathrm{s}}{\sigma_\mathrm{l}}$ defining the size ratio. In the case of an additive system [referred to as the hard-disk (HD) mixture], one may define an interaction diameter $d_{ij} = \sigma_i/2 + \sigma_j/2$ with $i, j = \{\mathrm{l},\mathrm{s}\}$. The pair potential $\Phi^{ij}(r)$ between two particles with center-center distance r is ∞ for $r < d_{ij}$ and 0 for $r > d_{ij}$.

In the case of an AO mixture, the interaction diameter d_{ss} for the interaction between two small disks is zero, i.e., there is no interaction among the small disks and they behave as an ideal gas. The other interaction diameters d_{sl} and d_{ll} remain unchanged. The small disks act as a depletant and induce an effective, attractive two-body potential $\Phi^{\mathrm{AO}}(r)$ between the large disks (depletion potential). Its shape is determined by the overlap of exclusion areas of two large disks at distance r, where the exclusion areas (which are forbidden to centers of small disks) are circles of diameter $\sigma_\mathrm{l} + \sigma_\mathrm{s}$ centered at the midpoints of the large disks [15,16]:

$$\beta\Phi^{\mathrm{AO}}(r) = \begin{cases} \infty & \text{if } r < \sigma_\mathrm{l} \\ -\eta'\left[\cos^{-1}\left(\frac{r}{\sigma_\mathrm{l}(1+q)}\right) - \frac{r}{\sigma_\mathrm{l}(1+q)}\sqrt{1-\left(\frac{r}{\sigma_\mathrm{l}(1+q)}\right)^2}\right] & \text{if } \sigma_\mathrm{l} < r < \sigma_\mathrm{l} + \sigma_\mathrm{s} \\ 0 & \text{otherwise,} \end{cases} \tag{1}$$

where $\eta' = \frac{\sigma_\mathrm{s}^2}{2}\rho_\mathrm{s}(\frac{1+q}{q})^2$ determines the magnitude of the depletion potential (ρ_s is the bulk number density of small disks). Furthermore, $\beta = \frac{1}{k_\mathrm{B}T}$, with k_B denoting Boltzmann's constant and T temperature. For small-size ratios $q < \frac{\sigma_\mathrm{s}}{\sigma_\mathrm{l}} \leqslant \frac{2-\sqrt{3}}{\sqrt{3}} \simeq 0.155$, the AO mixture can be mapped exactly onto a single-component model with an effective two-body potential given by the depletion potential above. For larger q, the effective potential should include n-body overlaps of excluded area ($n \geqslant 3$). Furthermore, in the dilute limit of the (additive) HD mixture (with the number density ρ_l of large disks being small), the effective potential between large disks is identical to Eq. (1) [15].

B. Fundamental measure theory

We consider inhomogeneous mixtures with density profiles $\rho(\mathbf{r}) = \{\rho_\mathrm{s}(\mathbf{r}), \rho_\mathrm{l}(\mathbf{r})\}$. In classical DFT, crystals are considered as inhomogeneous fluid, whose equilibrium density profile $\rho_{\mathrm{eq}}(\mathbf{r}) = \{\rho_{\mathrm{s,eq}}(\mathbf{r}), \rho_{\mathrm{l,eq}}(\mathbf{r})\}$ minimizes the grand potential

$$\Omega[\rho] = F[\rho] - \sum_i \int d\mathbf{r}\, \rho_i(\mathbf{r})[\mu_i - V_i^{\mathrm{ex}}(\mathbf{r})], \tag{2}$$

where F is the Helmholtz free energy, μ_i and V_i^{ex} are the chemical potential and the external potential for species i, respectively, and F can be further decomposed into the ideal gas part F_{id} and the excess free energy F_{ex}. The exact form of F_{id} is

$$\beta F_{\mathrm{id}} = \sum_{i=\{\mathrm{s,l}\}} \int d\mathbf{r}\, \rho_i(\mathbf{r})\left\{\ln\left[\rho_i(\mathbf{r})\lambda_i^2\right] - 1\right\}, \tag{3}$$

where λ_i is the thermal wavelength for species i. In the following, we set $\lambda_i = 1$.

Fundamental measure theory is the most accurate route to density functionals of hard-body mixtures. Most FMT functionals assume an excess-free-energy density which is local in a set of weighted densities $n_\alpha(\mathbf{r})$ which are convolutions of the density profiles with geometrically motivated weight functions [3]. For hard spheres in three dimensions, the original derivation of the functionals proceeds from an exact low-density form (deconvolution of the Mayer f bond) and subsequently uses scaled particle arguments [3]. Such a functional does not describe crystals though. In this case, a possible derivation proceeds via dimensional crossover. Here one requires that by confining an arbitrary density profile to one dimension (a line) and zero dimensions (a collection of points), the functional delivers the correct free energies whose exact form is known from other arguments [20,21]. Using this route, the properties of hard-sphere crystals and crystal-fluid interfaces are described in quantitative agreement with simulations [13,22,23]. Also, the low-density form remains exact.

In the derivation of a genuine 2D functional along these lines, problems are encountered. Maintaining the exact low-density form or having the exact free energy for a density distribution consisting of two sharp peaks is not possible with an excess-free-energy density local in weighted densities [20]. An approximate solution to this problem was derived in Ref. [4]. The excess free energy is given by

$$\beta F_{\mathrm{ex}}^{\mathrm{HD}}[n_\alpha] = \int d\mathbf{r}\, \Phi^{\mathrm{HD}}(n_\alpha), \tag{4}$$

where the weighted densities n_α are sums over convolutions of the HD species density profiles with weight functions

$$n_\alpha(\mathbf{r}) = \sum_{i=\{s,l\}} \int d\mathbf{r}'\rho_i(\mathbf{r}')w_\alpha^i(\mathbf{r}-\mathbf{r}') =: n_\alpha^s + n_\alpha^l, \tag{5}$$

where α indicates the type of weight function and i the species (l denotes large and s denotes small). The weight functions are defined as

$$\begin{aligned} w_1^i(\mathbf{r}) &= \delta(R_i - r), \quad w_0^i(\mathbf{r}) = \frac{\delta(R_i - r)}{2\pi R_i}, \\ w_2^i(\mathbf{r}) &= \Theta(R_i - r), \quad \mathbf{w}_1^i(\mathbf{r}) = \frac{\mathbf{r}}{r}\delta(R_i - r), \\ \left[\mathbf{w}_T^i(\mathbf{r})\right]_{\alpha\beta} &= \left(\frac{r_\alpha r_\beta}{\mathbf{r}^2}\right)\delta(R_i - r), \end{aligned} \tag{6}$$

where R_i is the radius of species i, $\theta(r)$ is the Heaviside step function, $\delta(r)$ is the Dirac delta function, and $\mathbf{w}_T^i(\mathbf{r})$ is a tensorial weight function with Cartesian components $\alpha\beta$.

The free-energy density is given by [4]

$$\Phi^{\mathrm{HD}}(n_\alpha) = -n_0\ln(1-n_2) + \frac{C_0 n_1^2 + C_1\mathbf{n}_1^2 + C_2\,\mathrm{Tr}\left[\mathbf{n}_T^2\right]}{4\pi(1-n_2)}, \tag{7}$$

with three parameters C_0, C_1, and C_2. The functional gives the correct second virial coefficient if $C_0 + C_2/2 = 1$. Furthermore, the correct free energy for a single sharp density peak requires $C_0 + C_1 + C_2 = 0$. Thus, the dependence on the three parameters can be reduced to a dependence on a single parameter a with

$$C_0 = \frac{a+2}{3}, \quad C_1 = \frac{a-4}{3}, \quad C_2 = \frac{2-2a}{3}. \tag{8}$$

For one component, a best fit to the Mayer f bond gives $a = 11/4$, whereas a fit to crystal pressures obtained by simulation gives $a = 3$ [4]. For binary systems in the fluid phase, the functional delivers an excellent description of pair correlation functions when compared to experiments [5].

Recently, a functional for 2D rods (discorectangles) has been derived which maintains the exact low-density form by using weighted densities which are two-center convolutions with a weight function [fundamental mixed measure theory (FMMT)] [24]. In the limit of the 2D rods becoming disks, the functional (7) is an approximation to the FMMT functional. However, fluid-crystal coexistence densities in the one-component case are approximately equal and the numerical effort in FMMT is considerably higher. Therefore, we will not consider the FMMT functional in this work.

A functional for the AO mixture can be obtained by the linearization recipe: A functional for a genuine hard-body mixture [such as the one in Eq. (7)] is linearized in the density (or equivalently in the weighted densities n_α^s) of the small species. This entails that the direct correlation function between two particles of the small species $c_{ss}^{(2)}(\mathbf{r},\mathbf{r}') = -\beta\delta^2 F_{ex}/\delta\rho_s(\mathbf{r})\delta\rho_s(\mathbf{r}')$ vanishes, consistent with the small species behaving as an ideal gas. In three dimensions, such a functional (derived from the original Rosenfeld functional [3]) describes structural properties and wetting transitions in the fluid phase very well [25]. Recently, an extension using functionals from the dimensional crossover route has been studied which allows the description of the crystal phase in three dimensions [19]. According to the linearization recipe, the AO mixture excess-free-energy density is given by

$$\Phi^{\mathrm{AO}}(\{n_\alpha^l, n_\alpha^s\}) = \Phi^{\mathrm{HD}}(n_\alpha^l) + \sum_\alpha n_\alpha^s \frac{\partial\Phi^{\mathrm{HD}}(n_\alpha^l)}{\partial n_\alpha^l}. \tag{9}$$

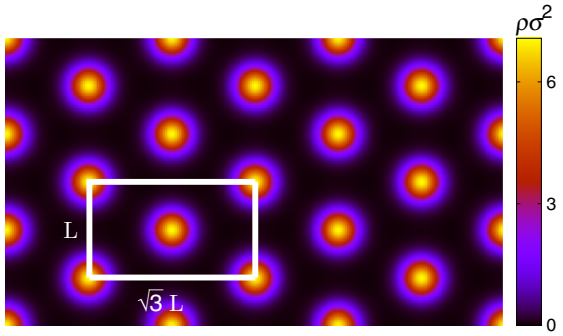

FIG. 1. Density distribution $\rho(\mathbf{r})$ of a one-component perfect crystal ($\bar{\rho}\sigma^2 = 0.93$ and $a = 11/4$). The solid white line indicates the computational box (rectangular unit cell of the triangular lattice, which contains two particles).

III. NUMERICAL METHODS

A. Free minimization and phase coexistence

For the crystal phase, we assume periodicity and consider a rectangular unit cell with side lengths L and $\sqrt{3}L$ for a triangular lattice (see Fig. 1). Since we only consider solid solutions (random disorder), we assume that the triangular lattice is formed by equilateral triangles as in the one-component case.

The free parameters in this free-energy minimization problem are the density profiles $\rho_l(\mathbf{r})$ and $\rho_s(\mathbf{r})$ in the unit cell as well as the length L. We parametrize the latter via an effective vacancy concentration n:

$$\int_{\mathrm{cell}} d\mathbf{r}[\rho_l(\mathbf{r}) + \rho_s(\mathbf{r})] =: 2(1-n) = (\bar{\rho}_l + \bar{\rho}_s)\sqrt{3}L^2. \tag{10}$$

In the one-component case, an ideal crystal has two particles in the unit cell, therefore $n > 0$ indeed corresponds to the vacancy concentration in the equilibrium crystal. For a HD mixture, n may also be negative, corresponding to an effective interstitial concentration which is easily possible if small disks are inserted into a crystal of large disks.

The full minimization for given average densities $\bar{\rho}_l$ and $\bar{\rho}_s$ proceeds via

$$F_{\mathrm{eq}}(\bar{\rho}_l, \bar{\rho}_s) = \min_n \min_{\{\rho_l(\mathbf{r}),\rho_s(\mathbf{r})\}} F[n_\alpha], \tag{11}$$

i.e., in two steps [22]. The first minimization step is achieved by an iterative solution of the Euler-Lagrange equation (for fixed n, L)

$$\rho_i = \exp\left(-\beta\frac{\delta F_{ex}[n_\alpha]}{\delta\rho_i} + \beta\mu_i\right) = K[\rho_i], \tag{12}$$

where

$$\beta\frac{\delta F_{\rm ex}[n_\alpha]}{\delta\rho_i(\mathbf{r})}=\int d\mathbf{r}'\sum_\alpha\frac{\partial\Phi[n_\alpha]}{\partial n_\alpha^i}(\mathbf{r}')w_\alpha^i(\mathbf{r}'-\mathbf{r}),\tag{13}$$

where Φ is given by Eq. (7) in the case of the HD mixture and by Eq. (9) in the case of the AO mixture. The chemical potentials μ_i are adapted in each iteration step to keep $\bar\rho_{\rm l}$ and $\bar\rho_{\rm s}$ constant. Iteration is done using a combination of Picard steps and discrete inversion in iterative subspace (DIIS) [13,22]. The Picard steps are performed according to

$$\rho_i^{j+1}=\xi K[\rho_i^j]+(1-\xi)\rho_i^j,\tag{14}$$

where i is the species index, j labels the iteration step, and ξ is a Picard mixing parameter which we chose in the range from 10^{-3} to 10^{-2} for bulk crystal and also interface minimizations. The DIIS steps are performed using between five and nine forward profiles. As a side remark, we also minimized $F[n_\alpha]$ by dynamic DFT with the exponential time differencing algorithm [26] for a one-component system. By choosing the time step $dt=10^{-3}$ (in units of the Brownian time σ^2/D_0, where D_0 is the single-particle diffusion constant), the thermodynamic properties in equilibrium are identical to the ones from the Picard-DIIS method, but the dynamic DFT method requires much more computational resources.

The second minimization step, the minimization with respect to n (and thus L), amounts to doing the first minimization for a few values of n within an interval of starting width $\sim10^{-3}$ and determining the minimum via a quadratic fit. The procedure is iterated with smaller interval widths until we have reached three digits of confidence or the interval width is less than 10^{-5}.

The procedure is slightly modified in the case of an AO mixture (see also Ref. [19] for more details). Here we define the vacancy concentration by

$$\int_{\rm cell}d\mathbf{r}\,\rho_{\rm l}(\mathbf{r})=:2(1-n)=\bar\rho_{\rm l}\sqrt{3}L^2,\tag{15}$$

i.e., it corresponds to the concentration of sites unoccupied by the large particles. Furthermore, we define a semigrand free energy (fixed $\bar\rho_{\rm l}$ and $\mu_{\rm s}$)

$$F'=F-\mu_{\rm s}\int d\mathbf{r}\,\rho_{\rm s}(\mathbf{r}),\tag{16}$$

which is minimized in step 1 for fixed n and L. In each iteration step, the density profile $\rho_{\rm s}(\mathbf{r})$ of the small spheres is computed by the grand-canonical equilibrium condition which can be solved explicitly:

$$\frac{\delta\Omega[\rho_{\rm l},\rho_{\rm s}]}{\delta\rho_{\rm s}}\overset{!}{=}0\Rightarrow$$

$$\rho_{\rm s}(\mathbf{r})=\exp\left(\beta\mu_{\rm s}-\int d\mathbf{r}'\sum_\alpha\frac{\partial\Phi_{\rm ex}^{\rm HD}[n_\alpha^{\rm l}]}{\partial n_\alpha^{\rm l}}w_\alpha^{\rm s}(\mathbf{r}'-\mathbf{r})\right).\tag{17}$$

Phase coexistence requires $P_{\rm cr}=P_{\rm fl}$ and $\mu_{\rm i,cr}=\mu_{\rm i,fl}$ with $i=$ l,s, i.e., coexisting fluid (crystal) states form two lines in the $\rho_{\rm l}$-$\rho_{\rm s}$ plane. In practice, first we choose $\rho_{\rm l}$ and $\rho_{\rm s}$ for the crystal and treat $\rho_{\rm l}=\rho_{\rm l,cr}$ as the parameter on which the other three coexistence densities depend. Fully minimizing F/N with n delivers $P_{\rm cr}$ and $\mu_{\rm i,cr}$. Through $\mu_{\rm i,cr}=\mu_{\rm i,fl}$ and the fluid equation of state we can find $P_{\rm fl}$, $\rho_{\rm l}$, and $\rho_{\rm s}$ in the fluid. In general, $P_{\rm fl}\neq P_{\rm cr}$ and thus we change $\rho_{\rm s,cr}$ iteratively until $\beta\sigma_{\rm l}^2|P_{\rm cr}-P_{\rm fl}|<5\times10^{-6}$.

B. Surface tension

A surface tension in two dimensions is a line tension defined as $\frac{\Omega+PA}{L}$, where P is the pressure, A is the area of the system and L is the length of the interface. In this paper we are interested in the planar surface tension γ, which is determined by the slope of the free-energy density versus the inverse length of the numerical box in the direction of the interface normal, with the average particle density fixed [27].

In general, γ depends on the angle θ between the crystal and the interfacial normal. For small anisotropies, γ can be approximated by $\gamma(\theta)=\gamma_0(1+\epsilon\sin(6\theta))$; in FMT, $\epsilon\simeq O(10^{-3})$ for the one-component crystal-fluid interface. In experiments [2], $\epsilon\simeq O(10^{-2})$. Due to the smallness of ϵ, in this paper γ_0 is directly determined by $\frac{\gamma(0)+\gamma(\pi/6)}{2}$.

The density profiles are initialized similar to Ref. [13]. In the iterations we chose a Picard mixing parameter constant in space (this works here in two dimensions but not in three [13]). We fix the average densities $\bar\rho_i=\frac{\bar\rho_{i,\rm cr}+\bar\rho_{i,\rm fl}}{2}$ by adapting μ_i in the iterations, where $\bar\rho_{\rm i,cr\,(fl)}$ is the bulk average density in the crystal (fluid) phase for species i at coexistence, and then finally perform the free minimization.

C. Further numerical details

Here we briefly discuss further computational details. The crystal phase requires double precision, with numbers of grid points from 64^2 up to 256^2 for one unit cell. The crystal-fluid interfaces require an extension of the numerical box between 1×96 and 1×196 unit cells to give reliable surface tensions. Heavy usage of Fourier transforms is required for the minimization. Weighted densities (6) are computed using

$$\mathfrak{F}(n_\alpha^i)=\mathfrak{F}(\rho^i)\mathfrak{F}(w_\alpha^i)\tag{18}$$

and functional derivatives (13) by

$$\mathfrak{F}\left(\frac{\delta F_{\rm ex}[n_\alpha]}{\delta\rho_i}\right)=\sum_\alpha\mathfrak{F}\left(\frac{\partial\Phi_{\rm ex}[n_\alpha]}{\partial n_\alpha^i}\right)\mathfrak{F}^\star(w_\alpha^i),\tag{19}$$

with $\mathfrak{F}$ denoting the Fourier transform and the star the complex conjugate. For $\mathfrak{F}(w_\alpha)$, the analytic forms using Bessel functions are used [28]. For accelerating the numerics, all calculations are executed on high-performance Nvidia Tesla K80 or K40 GPUs with massive parallelization through the developer environment CUDA [29]. For a detailed description of GPU utilization in two- and three-dimensional FMT, we refer the reader to the paper by Stopper and Roth [28]. CUDA has a wide range of tools and libraries, such as template library thrust and fast Fourier transforms (cuFFT) which is usually a bottleneck in the DFT calculations. With a potential speed gain of up to 40 times relative to a serial CPU program [28], our calculations gave a factor of 15–20 since we try to maximize the system size; thus, our largest system is 4 times larger than those in Ref. [28]. The minimization of a unit cell (first minimization step) usually takes a few seconds (~500 Picard-DIIS steps)

TABLE I. Thermodynamic properties of the one-component crystal-fluid transition: γ_0 denotes the averaged planar surface tension, σ the HD diameter, μ chemical potential, P pressure, $\eta = (\pi/4)\sigma^2\rho$ packing fraction, superscript 1c one component, and subscript co the coexistence of the crystal (cr) and fluid (fl). Note that for Expt. and MC, two values for η_{cr} correspond to the packing fraction of the hexatic phase at fluid-hexatic coexistence and the packing fraction at the hexatic-crystal continuous transition, respectively. The FMT coexistence values for $a = 11/4$ differ slightly from those in Ref. [4], which suffer from a small numerical error. The results of the experiment in column 4 are from Ref. [2] (see Supplemental Material therein) and those of the MC simulations in column 5 are from Ref. [1].

	FMT			
Property	$a = 11/4$	$a = 3$	Expt.	MC
$\beta\sigma\gamma_0^{1c}$	0.0992	0.0815	0.1	
$\beta\sigma^2 P_{co}^{1c}$	10.84	9.234		9.185
$\beta\mu_{co}$	14.576	12.778		
η_{cr}^{1c}	0.732	0.7165	0.7/0.73	0.716/0.72
η_{fl}^{1c}	0.711	0.6913	0.68	0.700

and that of an interface about 15–30 min (∼5000 Picard-DIIS steps) for one-component system.

IV. RESULTS

A. One-component system

In the past decade, two-dimensional one-component HD systems were extensively studied, with now quantitative agreement in type and location of the phase transition between experiments [2] and Monte Carlo (MC) simulations [1]. For a summary, in Table I we provide a comparison between FMT, MC simulations, and experiments. Experiments and simulations find a first-order transition between the fluid and the hexatic phase, and a continuous transition between the hexatic and crystal phase. The surface tension in the experiments [2] (see the Supplemental Material therein) is for hexatic-fluid coexistence. The FMT results are for an assumed first-order transition between fluid and crystal.

From Table I we see that coexistence packing fractions and the surface tension are described very well by FMT, even though in FMT the strict periodicity assumption for the crystal differs from the character of the hexatic and crystal phase in experiments or simulations. This good correspondence is in line with the quantitative description of fluid structure given in earlier work [4,5].

B. Binary systems: Crystal density profiles

When the radii of the disks are comparable (large $q \lesssim 1$), we observe a clear substitutional disorder. Density peaks for both species are centered on the triangular lattice points and their magnitude is essentially determined by the composition of the crystal. An example can be seen in the crystal part of the crystal-fluid density profile shown in Fig. 7 with $q = 0.75$.

For small-size ratios $q \ll 1$, we observe interstitial disorder, i.e., the small disks almost exclusively occupy the interstitial space between the large disks which in turn occupy the triangular lattice points. An example can be seen in the crystal part of the crystal-fluid density profile shown in Fig. 7 with $q = 0.15$. The HD and AO case are very similar, and qualitatively the AO crystal density profiles in three dimensions show the same behavior [19].

For intermediate q and the HD case, we observe a superposition of substitutional and interstitial disorder, and the interstitial disorder may show a transition to different alloy configurations upon changing the composition. We exemplify this for $q = 0.45$. Large-disk density peaks are again centered on the triangular lattice positions (not shown). For low small-disk concentrations [see Fig. 2(a)], we observe interstitial disorder superficially compatible with an AB_2 structure. From the large and small disks drawn in Fig. 2(a) one sees however that the small disks are too big for the formation of a true AB_2 phase. For higher small-disk concentrations [see Fig. 2(b)] the lattice constant becomes smaller (large spheres on the triangular lattice points almost touch) and the interstitial density peaks of the small spheres are compatible with an AB_3 structure. Here, remarkably, the large disks drawn around the triangular lattice points and the small disks drawn around the interstitial peak positions reveal two packed AB_3 configurations. In the AO case, we only observed a small-disk density distribution of the type of Fig. 2(a).

Here we have not investigated whether the minimized crystal structures with disorder are stable or not with respect to phase separation into different alloy phases. This requires

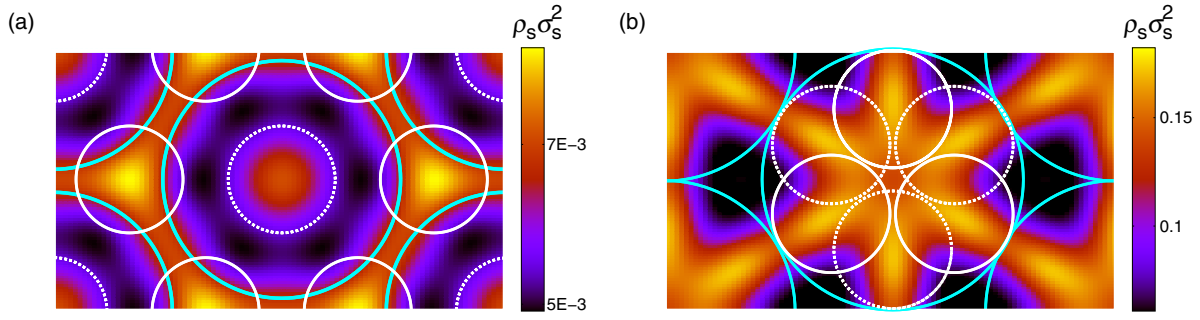

FIG. 2. Density profiles for small disks in a HD mixture crystal with $q = 0.45$ at crystal-fluid coexistence for small disk concentration (a) $c_s = 0.03$ and (b) $c_s = 0.39$, with $c_s = \rho_s/(\rho_s + \rho_l)$. The solid blue circles indicate the extension of large disks; solid and dashed white circles indicate the extension of small disks. In both cases, the density profile is a superposition of substitutional and interstitial disorder. In (b), interstitial disorder dominates and is compatible with an AB_3 alloy structure where one large disk is replaced by three small disks (white solid or dashed circles).

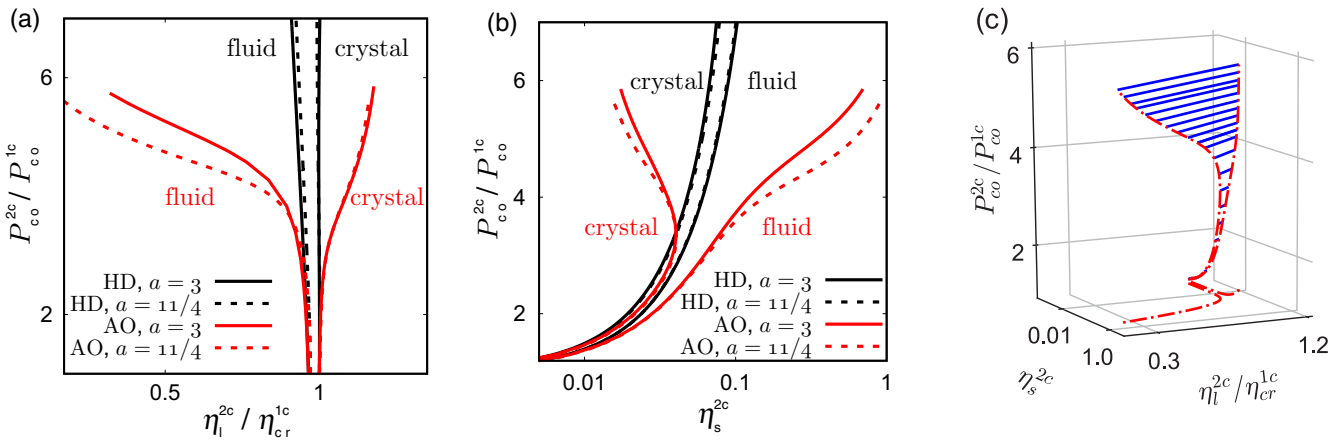

FIG. 3. Phase diagram for the size ratio $q = 0.15$ in (a) the η_l-P plane, (b) the η_s-P plane, and (c) the three-dimensional η_l-η_s-P space (only for an AO mixture with $a = 11/4$). In (c), the blue lines are tie lines and the projection of the phase diagram onto the η_l-η_s plane is also shown. The pressure P_{co}^{2c} and packing fraction of large disks η_l^{2c} are normalized by the coexistence values of the one-component HD system P_{co}^{1c} and η_{cr}^{1c}.

more extensive investigations beyond the scope of this work. However, our results illustrate that a free minimization of the FMT functional is capable of generating alloy structures without the need to explicitly parametrize the density profiles (e.g., by suitably chosen Gauss peaks, as it is often done).

C. Binary systems: Phase diagrams

For two-component hard systems, equilibrium states are on a surface in a three-dimensional space, spanned by, e.g., the packing fractions η_l and η_s and the pressure P. Consequently, binodals are lines in this three-dimensional space and they are often displayed by their two-dimensional projections, e.g., lines in the η_l-P or $c_{s/l}$-P plane where $c_{s/l} = \rho_{s/l}/(\rho_l + \rho_s)$ is the relative concentration of small/large spheres. In the AO model, customarily the η_l-μ_s plane is chosen but the topology of phase diagrams is very similar to the one in the η_l-P plane.

1. Small-size ratios q

For a size ratio $q = 0.15$, the phase diagram is shown in Fig. 3 in two different projections. For both HD and AO mixtures, the addition of the small species leads to an increased coexistence pressure for the fluid-crystal transition, i.e., the fluid phase is stabilized. The AO mixture shows the typical widening of the coexistence gap ($\eta_{l,cr} - \eta_{l,fl}$) with increasing concentration of the small species (see Fig. 3), smoothly leading to a sublimation line. For $\eta_s \lesssim 0.01$, the HD mixture binodal follows the AO binodal, i.e., also shows an initial widening of the coexistence gap. This could be expected since for these small concentrations the small disks only act as depletants and their mutual interaction is irrelevant. For higher η_s, the binodals separate. The choice of the parameter a in the functional has a significant influence on the location of the binodal. This is similar to the observation in Ref. [19] that also in the 3D case, the binodal differs considerably between the White Bear II (tensor) and the Rosenfeld (tensor) functional,

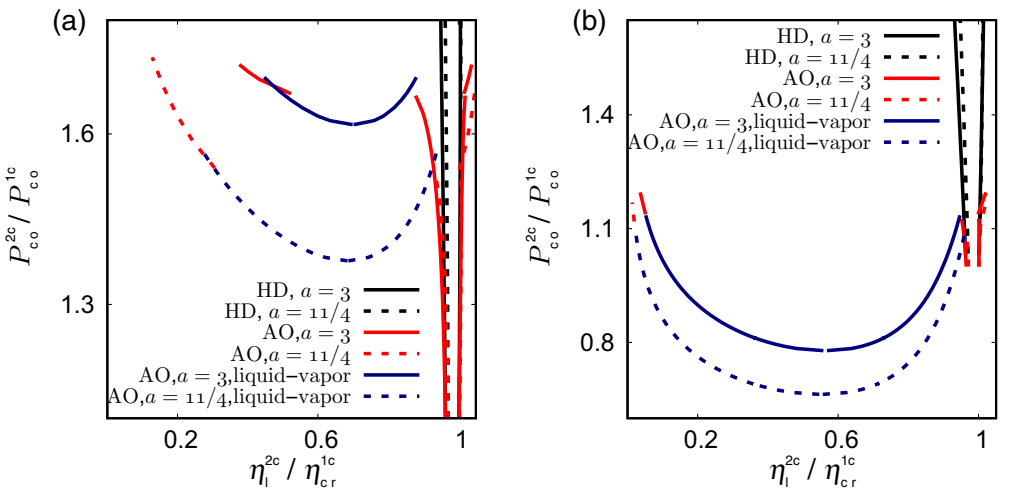

FIG. 4. Binary mixture phase diagrams for (a) $q = 0.3$ and (b) $q = 0.45$ in the η_l-P plane. Pressure and packing fraction are normalized by the coexistence values of the one-component HD system P_{co}^{1c} and η_{cr}^{1c}.

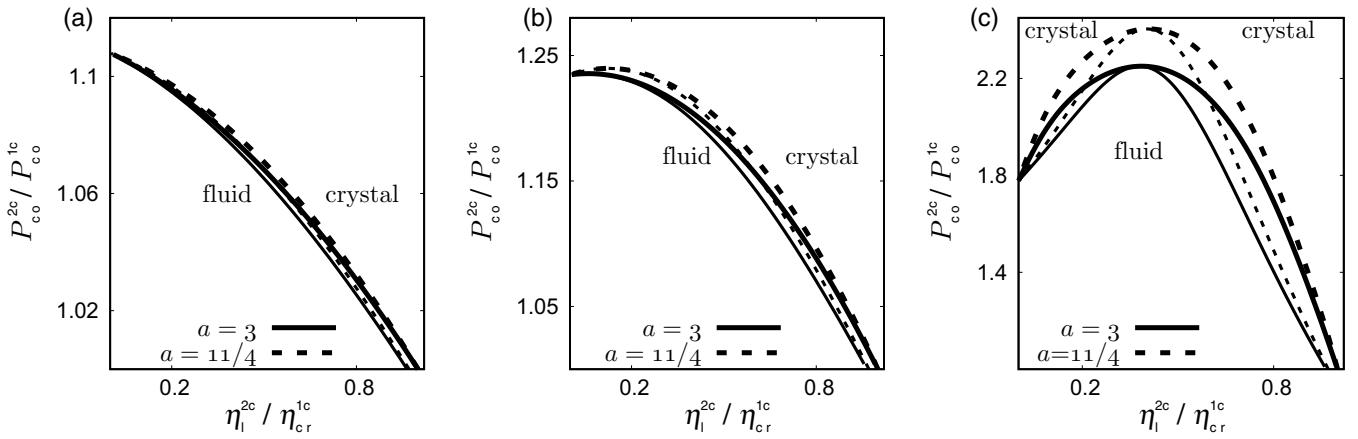

FIG. 5. Hard-disk mixture phase diagrams for (a) $q = 0.95$, (b) $q = 0.9$, and (c) $q = 0.75$ in the η_l-P plane. Thick (thin) lines show crystal (fluid) states at coexistence.

although the differences in the one-component case are not that significant.

For the size ratios $q = 0.3$ and $q = 0.45$, the phase diagrams are shown in Fig. 4 in the η_l-P plane. For the AO mixture, the liquid (rich in large disks) to vapor (poor in large disks) transition has become stable. The difference in the location of the liquid-vapor transition between the FMT results for the two different values of a is only a consequence of normalizing the pressure axis by P_{co}^{1c} (for the two a values, it differs by $\sim$15%; see Table I). For the HD mixtures, there is no fluid-fluid transition and there is hardly any widening of the coexistence gap of the fluid-crystal transition visible.

The results for the AO mixture are very similar to the 3D case [19]. Experimentally, it is possible to realize such 2D systems by sedimented monolayers of colloidal spheres (as in Refs. [2,5]) to which nonadsorbing polymers can be added. For small-size ratios $q \lesssim 0.15$ it would be interesting to study experimentally or by simulations the fate of the established melting scenario for hard disks as the polymer concentration is increased. As we have seen, the coexistence gap continuously widens in this case, and we expect that towards the sublimation regime only the first-order transition survives.

2. Size ratios q close to 1

For size ratios q in the vicinity of 1, we only focus on the HD mixture. In the AO mixture, the phase diagram becomes rather uninteresting with regard to crystal phases. There, upon addition of the smaller, polymeric component, the one-component crystal does not change very much: The polymers fill up the vacancies until the triple point is reached and the fluid-crystal transition becomes unstable with respect to sublimation. Again, this is very similar to the 3D case, and a detailed discussion can be found in Ref. [19].

For HD mixtures, phase diagrams are shown in Fig. 5. For q very close to 1, the phase diagram is of a type commonly referred to as spindle type (which would be directly visible in the c_l-P plane or in the c_s-P plane): The coexistence pressure continuously increases upon addition of smaller disks and reaches its maximum for the pure small-disk system [see Fig. 5(a)]. Upon lowering q, the type of phase diagram crosses over to azeotropic [see Figs. 5(b) and 5(c)]: There a maximum pressure for a stable fluid is found for a certain finite composition, i.e., for a truly mixed system. At this point of maximum pressure, the coexisting fluid and crystal have the same composition (azeotropic point). The precise value for q

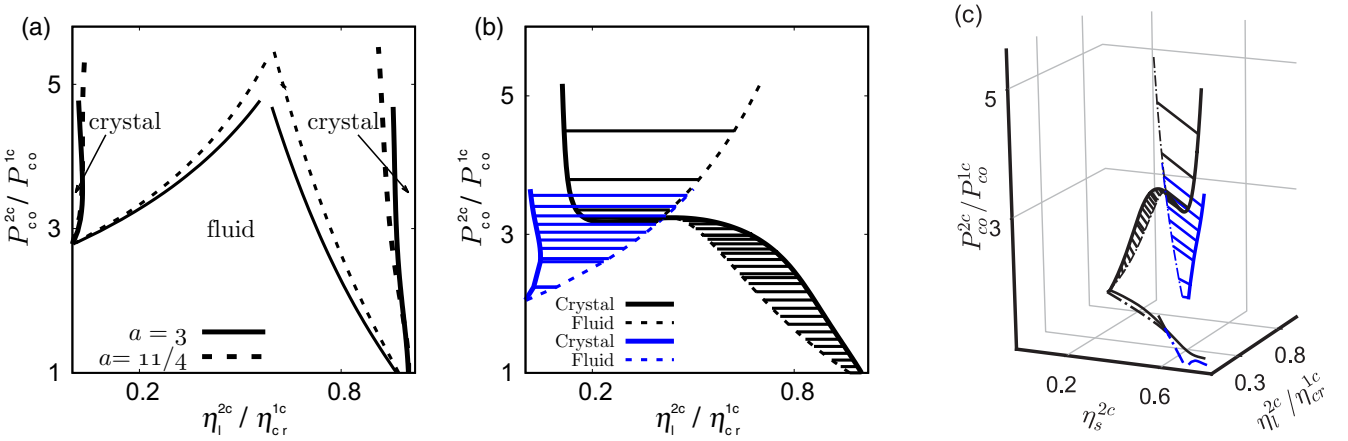

FIG. 6. Hard-disk mixture phase diagrams for (a) $q = 0.6$ and (b) and (c) $q = 0.7$ with $a = 3$.

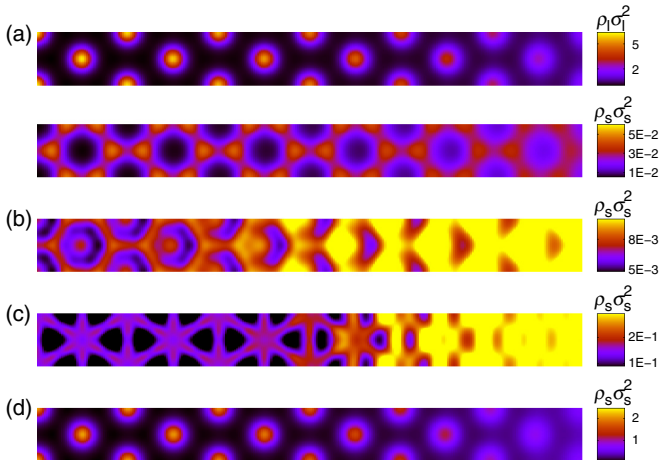

FIG. 7. Hard-disk mixture density profiles ρ for the cross crystal (left)-fluid (right) interface for (a) $q = 0.15$ and $c_s = 0.5$, (b) $q = 0.45$ and $c_s = 0.03$, (c) $q = 0.45$ and $c_s = 0.39$, and (d) $q = 0.75$ and $c_s = 0.52$. Here c_s refers to the concentration of small disks in the crystal at coexistence. Since all large disk density profiles looks similar, here we only show a representative one.

where this transition happens depends on the parameter a in the functional; it is around 0.91 for $a = 3$ and around 0.93 for $a = 11/4$. The transition from spindle type to azeotropic phase diagrams has also been observed in simulations of hard-sphere mixtures in three dimensions [8]. There the transition happens at around $q = 0.94$. Furthermore, in three dimensions the azeotropic phase diagram changes to a eutectic phase diagram already at around $q = 0.88$. From our results, this happens in two dimensions at much lower q (discussed below).

3. Intermediate-size ratios q

Again we will only discuss HD mixtures. The phase diagrams for $q = 0.6$ and $q = 0.7$ are shown in Fig. 6. For $q = 0.6$, we observe a phase diagram of eutectic type. It is actually very similar to the phase diagram found in simulations for $q = 1/1.4$ (see Supplemental Material in Ref. [14]). The crossover to the azeotropic phase diagram (as seen for $q = 0.75$ in Fig. 5) is surprising according to the FMT results.

For $q = 0.7$, a three-dimensional phase diagram in η_l-η_s-P space is shown in Fig. 6. The coexisting plane with a majority of large disks (black surface) is close to the one of small disks (blue surface), but does not cross (see the projection onto the η_l-η_s plane). By increasing q, two planes merge and then form an azeotropic type. Back to the η_l-P plane, the branch with a majority of large disks distorts to form an azeotropic point (see the black lines in Fig. 6 for $q = 0.7$), whereas the branch with a majority of small disks remains approximately unchanged when compared with $q = 0.6$. Thus, above the azeotropic point pressure there is a stable and a metastable coexistence between a crystal with a majority of small disks and a mixed fluid.

D. Binary systems: Interface density profiles

Figure 7 shows representative density profiles of the crystal-fluid interface for hard-disk mixtures with $q = 0.15, 0.45$, and 0.75. For all size ratios q, the density of large disks is always peaked on the triangular lattice sites [see Fig. 7(a)] while the density of small disks changes from interstitial to substitutional disorder by increasing q (see also the discussion in Sec. IV B). For the AO mixture, we found similar density profiles for $q < 0.5$, except Fig. 7(c). From the profiles one infers a rather broad interface.

We analyze the interface structure further by employing the methods of Ref. [30]. Smooth average density and crystallinity modes can be extracted from the Fourier transform of the full density profiles by picking a lateral reciprocal lattice vector $\mathbf{K}_y$ and cutting out a window around a reciprocal lattice vector $\mathbf{K}_x$ parallel to the interface normal. The average modes are the inverse Fourier transforms of the cutout window. The average density mode M_0 is obtained by choosing $\mathbf{K}_x = \mathbf{K}_y = 0$ and the leading crystallinity mode M_1 is obtained by choosing $\mathbf{K}_y = 0$ and $\mathbf{K}_x = 4\pi/\sqrt{3}L$, where L is the length of the rectangular unit cell side which is parallel to the interface (see Figs. 2 and 7). In general, M_1 is complex; in figures we show its absolute value only. As a rule of thumb, M_0 represents an averaged density profile with oscillations smoothed out and M_1 the amplitude of oscillations.

In Fig. 8 we compare laterally averaged density profiles with the extracted density and crystallinity modes for the four interfaces of Fig. 7. Several observations can be made. First, looking at the density and crystallinity mode of large disks (middle column in Fig. 8) we note that coming from the fluid side, crystallinity sets in earlier as densification (except for the case $q = 0.45$ and $c_s = 0.39$). This has also been noted before in the 3D case of one-component hard spheres [30]. Second, looking at the density and crystallinity mode of small disks (right column in Fig. 8), we observe that for small $q = 0.15$ (interstitial disorder) and large $q = 0.75$ (substitutional disorder) the small-disk crystallinity is essentially proportional to the large-disk crystallinity. Since the crystal has a smaller concentration of small disks than in the fluid, the density mode increases from left to right but stays monotonic. For the intermediate-size ratio $q = 0.45$ we note that the crystallinity of small disks is peaked at the interface and for $c_s = 0.39$ this also applies to the density mode. Thus we see an interfacial enrichment of ordered small spheres. This interfacial enrichment can be also seen in the laterally averaged density profiles (left column in Fig. 8) which exhibit an increase in the oscillation amplitude of the small sphere density (red lines) in the interfacial region. However, the quantification of this effect is easier using the crystallinity and density modes.

E. Binary systems: Crystal-fluid surface tensions

1. Size ratio q $\leqslant$ **0.6**

For small- to moderate-size ratios of up to 0.6, we may view the small disks as depletants, at least for small concentrations c_s. In Fig. 9 we show the associated crystal-fluid planar surface tension γ_0^{2c} versus c_s for both AO and HD mixtures. For $q = 0.15$, we have computed the surface tension for c_s up to 0.85. We remind the reader of the associated phase diagrams (Fig. 3) which in the AO case show the typical widening of the coexistence gap. In the HD case, the widening of the coexistence gap follows the AO case only for small c_s. It is a bit surprising that the surface tension *decreases*

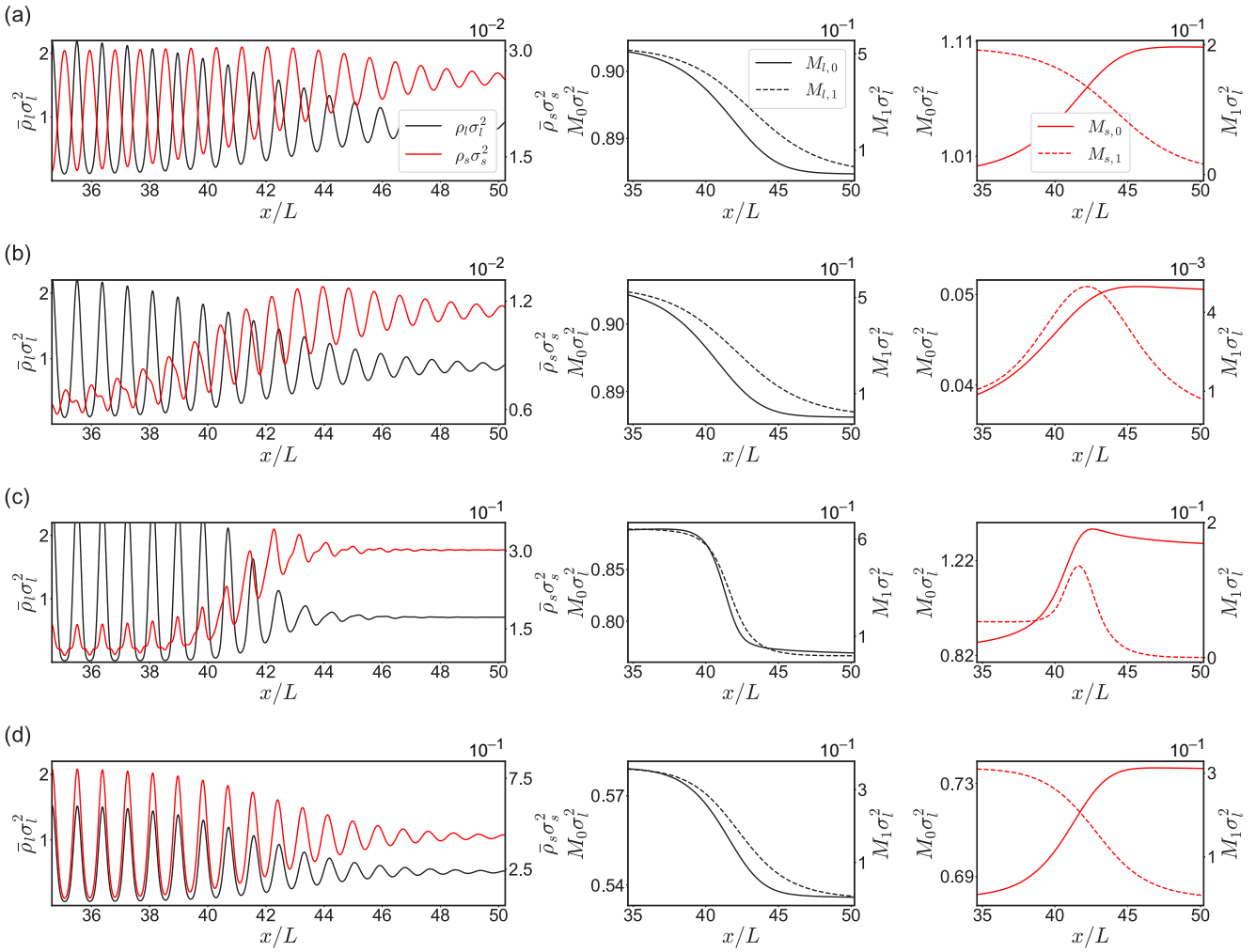

FIG. 8. Laterally averaged density profiles (left column) and density and leading crystallinity modes of large disks (middle column) and small disks (right column) for the four interfaces of Fig. 7: (a) $q = 0.15$ and $c_s = 0.5$, (b) $q = 0.45$ and $c_s = 0.03$, (c) $q = 0.45$ and $c_s = 0.39$, and (d) $q = 0.75$ and $c_s = 0.52$. Here c_s refers to the concentration of small disks in the crystal at coexistence. Black lines refer to large disks and red lines to small disks. In the middle and right columns, solid lines are density modes M_0 and dashed lines are crystallinity modes M_1.

upon addition of small disks, with the results for the HD mixture on top of those for the AO mixture until $c_s \sim 0.4$. In the depletion picture, the addition of small disks leads to an increasing attraction between large disks. In mean-field approximation, the increasing attraction, together with an increasing coexistence gap, should lead to a higher surface tension. Such an increase is seen for both the AO model and the HD case only for rather large c_s, after a minimum has been reached around $c_s \approx 0.6$. In the HD case, for $c_s \to 1$ we reach the monocomponent case for small disks, thus the surface tension should reach $\gamma_0^{2c}(c_s = 1) = \frac{\sigma_l}{\sigma_s}\gamma_0^{2c}(c_s = 0) = \gamma_0^{1c}/q$. The decrease in surface tension upon addition of a second component is actually typical for surfactant systems. From the Gibbs adsorption equation in binary systems one finds such a decrease if there is an enrichment of the second component at the interface (net adsorption greater than 0 if the interface is chosen as the equimolar surface for the first component [31]). Such a behavior occurs here; it is seen markedly for $q = 0.45$ [Fig. 8(c), solid red lines]. As a side remark, in square gradient theory for binary liquids, the decrease of surface tension upon addition of the second species is only describable using mixing parameters reflecting a substantial nonadditivity in the system [32].

The peculiar behavior of an initially decreasing surface tension is also seen for $q = 0.3$, $q = 0.45$, and $q = 0.6$ (see Fig. 9), although the decrease becomes smaller with increasing q. With increasing size ratio, also the HD and the AO results differ more and more already for small c_s and we also note that the choice of the parameter a in the FMT functional influences the results considerably. Overall, the surface tensions are rather small on the thermal energy scale. For the monocomponent case this leads to strong interface fluctuations, as observed in Ref. [2]. Owing to the decrease in γ_0^{2c} upon addition of small disks, we would expect that these fluctuations also become stronger.

2. *Size ratio $q \geqslant 0.75$: Hard-disk mixtures*

For $q \geqslant 0.75$, the phase diagram in the HD mixture is of azeotropic or spindle type (see Fig. 5), thus we can determine

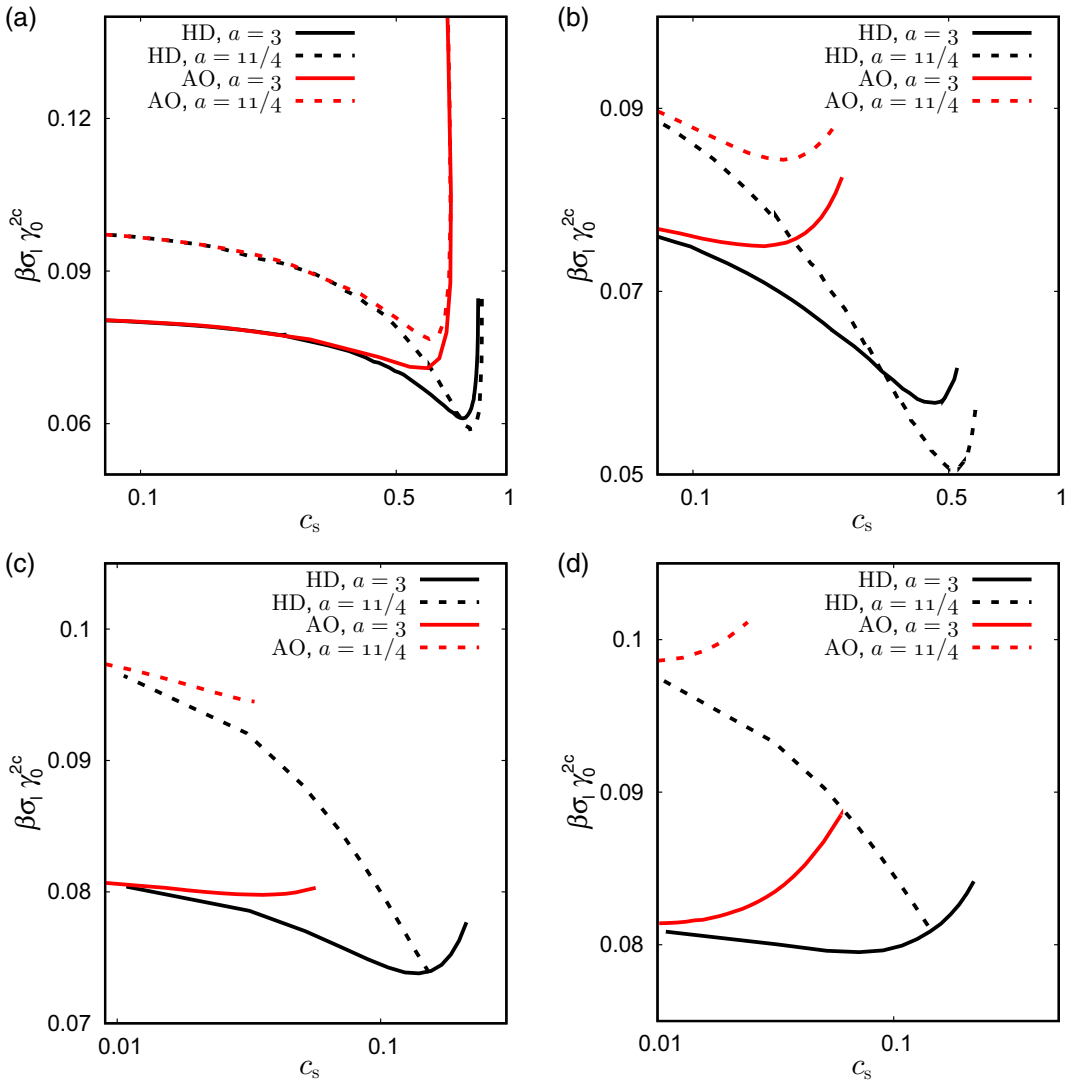

FIG. 9. Crystal-fluid surface tension γ_0^{2c} for the AO and the HD case, two values of a, and (a) $q = 0.15$, (b) $q = 0.3$, (c) $q = 0.45$, and (d) $q = 0.6$. Here c_s refers to the concentration of small disks in the crystal at coexistence. Note that c_s is in logarithmic scale.

γ_0^{2c} in the whole range of concentrations from $c_s = 0$ up to 1. In Fig. 10, the surface tension γ_0^{2c} versus c_s is shown for four aspect ratios $q \geqslant 0.75$ and the two values of the parameter a. Qualitatively, there is no significant dependence on a for these size ratios. As before (for small q), the initial decrease of γ_0^{2c} for small c_s is present. There is a minimum in the surface tension around $c_s = 0.5$ and it reaches the correct monocomponent value $\gamma_0^{2c}(c_s = 1) = \gamma_0^{1c}/q$.

The surface tensions can actually be well described with the function involving one fit parameter κ,

$$\gamma_0^{2c}([\eta_{cr}],q) = \frac{\gamma_0^{1c}}{\left(\eta_{cr}^{1c}\right)^2}\left((\eta_{l,cr})^2 + \frac{(\eta_{s,cr})^2}{q} + \kappa\eta_{l,cr}\eta_{s,cr}\right), \tag{20}$$

where γ_0^{1c} and η_{cr}^{1c} on the right-hand side of Eq. (20) are the monocomponent surface tension and the coexistence crystal packing fraction (see Table I) and $\eta_{l/s,cr}$ are the coexistence crystal packing fractions of large and small hard disks. For the fit parameter κ we note that $\lim_{q\to 1}\kappa(q) = 2$. For $q < 0.75$, Eq. (20) is not valid, which may be due to the complicated transition from an azeotropic to a eutectic phase diagram (as discussed before). Equation (20) is a semiempirical function, and similar forms can be found in older work on surface tensions in binary system which aimed at parametrizing the effect of interfacial adsorption [33,34].

V. CONCLUSION

Using density-functional theory (fundamental measure theory), we have performed an extensive study of the phase diagram and crystal-fluid surface tensions in binary hard-disk systems, for both the additive case and the nonadditive (Asakura-Oosawa like) case. Since we assumed a periodic crystal, we find first-order transitions only. These correspond to the first-order fluid-hexatic transition for the one-component case and presumably to first-order fluid-crystal transitions (which become stable upon admixing a second component; see, e.g., Ref. [14]). Overall, the phase diagrams are qualitatively very similar to the 3D case. In the AO case and for small-size ratios q, the typical continuous widening of the coexistence

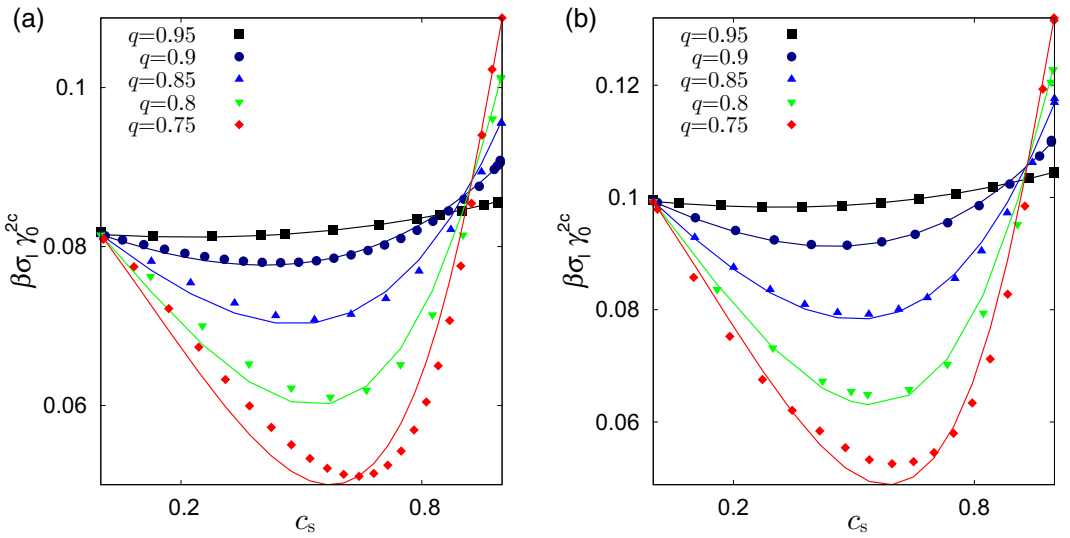

FIG. 10. Crystal-fluid surface tension γ_0^{2c} for the HD case, size ratios $q \geqslant 0.75$, and (a) $a = 3$ and (b) $a = 11/4$. Symbols are the numerical results and the lines are best fits to Eq. (20).

gap is observed upon addition of the smaller species, and for intermediate q a vapor-liquid transition becomes stable. In the additive case, the phase diagrams show the sequence spindle to azeotropic to eutectic upon lowering q from 1 to 0.6 (similar to the 3D case). However, the transition from azeotropic to eutectic is different from what is known in 3D hard-sphere systems (see the phase diagram in Fig. 6 for $q = 0.7$).

The results for the crystal-fluid surface tensions reveal two things. Overall, their values are much smaller than 1 in thermal units $1/\beta\sigma_l$. For the one-component case, the resulting large thermal fluctuations of the interface have been observed experimentally [2]. Further, the addition of a second component leads in general to a substantial decrease in the surface tension. This holds for the AO case (for $q \lesssim 0.6$) and also for the additive case (here for the whole range of q). Complementary dedicated simulation or experimental results on this are clearly desirable, also in view of the relevance of the surface tension for nucleation processes (see Ref. [35] for a review on more qualitative results on 2D crystal and defect formation). The observed decrease in surface tension should lead to a considerable decrease in the timescales of crystal nucleation.

In contrast to phase diagrams, results on crystal-fluid surface tensions in binary 3D systems are scarce. For binary hard spheres with a size ratio of $q = 0.9$, results are reported in Ref. [36]. For that q, the phase diagram is azeotropic. The surface tension is found to increase monotonically with the addition of small spheres. These findings are similar to those for a 3D binary Lennard-Jones system with zero-size mismatch but a ratio of interaction strengths of 0.75 (leading to a spindle-type phase diagram) [37], but they are different from the nonmonotonic behavior found here in the 2D system (see Fig. 10).

The full minimization of the FMT functionals shows interesting effects for the density distributions in the crystal unit cells and of the crystal-fluid interfaces. For intermediate-size ratios (examples shown for $q = 0.45$) superpositions of substitutional and alloy structures are found, and enhanced crystallinity and density of small disks are observed right at the interface between crystal and fluid. Clearly, an extension of the present studies to the global stability of alloy phases and their interfaces is desirable but requires considerably more efforts.

ACKNOWLEDGMENTS

S.-C.L. thanks Landesgraduiertenförderung Baden-Württemberg for financial support. The authors acknowledge support from the High Performance and Cloud Computing Group at the Zentrum für Datenverarbeitung of the University of Tübingen, the state of Baden-Württemberg through bwHPC, and the German Research Foundation through Grant No. INST 37/935-1 FUGG.

APPENDIX: LIQUID-VAPOR SURFACE TENSION

For completeness, we present also results for the liquid-vapor surface tension γ_{lv} versus $\Delta\eta_l$ in the AO model for size ratios $q = 0.3, \ldots, 0.7$, where $\Delta\eta_l = \eta_{l,liq} - \eta_{l,vap}$ is the

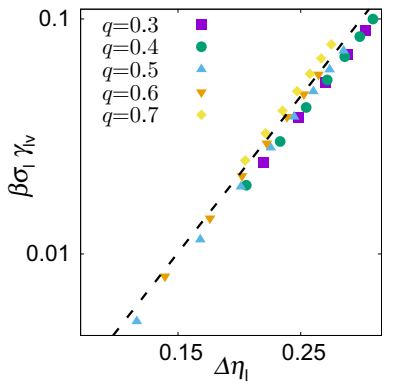

FIG. 11. Double logarithmic plot of γ_{lv} versus $\Delta\eta_l$. The dashed line shows $\gamma_{lv} \propto (\Delta\eta_l)^3$.

difference between the coexistence packing fractions of large disks in the liquid and vapor phases (see Fig. 11). Similar to the crystal-fluid surface tension, the numerical values for γ_{lv} are much smaller than 1 in thermal units $1/\beta\sigma_1$, even far away from the critical point. For mean-field models, the assumed power-law relation $\gamma_{\mathrm{lv}} \propto (\Delta\eta_{\mathrm{l}})^3$ is found to hold not only in the immediate vicinity of the critical point. This is similar to results from density-functional studies of the 3D AO model [38].

[1] E. P. Bernard and W. Krauth, Phys. Rev. Lett. **107**, 155704 (2011).
[2] A. L. Thorneywork, J. L. Abbott, D. G. A. L. Aarts, and R. P. A. Dullens, Phys. Rev. Lett. **118**, 158001 (2017).
[3] Y. Rosenfeld, Phys. Rev. Lett. **63**, 980 (1989).
[4] R. Roth, K. Mecke, and M. Oettel, J. Chem. Phys. **136**, 081101 (2012).
[5] A. L. Thorneywork, R. Roth, D. G. A. L. Aarts, and R. P. A. Dullens, J. Chem. Phys. **140**, 161106 (2014).
[6] X. C. Zeng, D. W. Oxtoby, and Y. Rosenfeld, Phys. Rev. A **43**, 2064 (1991).
[7] H. Xu and M. Baus, J. Phys.: Condens. Matter **2**, 5885 (1990).
[8] W. G. T. Kranendonk and D. Frenkel, Mol. Phys. **72**, 679 (1991).
[9] C. N. Likos and C. L. Henley, Philos. Mag. B **68**, 85 (1993).
[10] K. R. Elder, N. Provatas, J. Berry, P. Stefanovic, and M. Grant, Phys. Rev. B **75**, 064107 (2007).
[11] M. Greenwood, N. Ofori-Opoku, J. Rottler, and N. Provatas, Phys. Rev. B **84**, 064104 (2011).
[12] N. Provatas and S. Majaniemi, Phys. Rev. E **82**, 041601 (2010).
[13] M. Oettel, S. Dorosz, M. Berghoff, B. Nestler, and T. Schilling, Phys. Rev. E **86**, 021404 (2012).
[14] J. Russo and N. B. Wilding, Phys. Rev. Lett. **119**, 115702 (2017).
[15] R. Castaneda-Priego, A. Rodríguez-López, and J. Méndez-Alcaraz, J. Phys.: Condens. Matter **15**, S3393 (2003).
[16] S. Asakura and F. Oosawa, J. Chem. Phys. **22**, 1255 (1954).
[17] S. Asakura and F. Oosawa, J. Polym. Sci. **33**, 183 (1958).
[18] M. Schmidt, H. Löwen, J. M. Brader, and R. Evans, Phys. Rev. Lett. **85**, 1934 (2000).
[19] M. Mortazavifar and M. Oettel, J. Phys.: Condens. Matter **28**, 244018 (2016).
[20] P. Tarazona and Y. Rosenfeld, Phys. Rev. E **55**, R4873 (1997).
[21] P. Tarazona, Phys. Rev. Lett. **84**, 694 (2000).
[22] M. Oettel, S. Görig, A. Härtel, H. Löwen, M. Radu, and T. Schilling, Phys. Rev. E **82**, 051404 (2010).
[23] A. Härtel, M. Oettel, R. E. Rozas, S. U. Egelhaaf, J. Horbach, and H. Löwen, Phys. Rev. Lett. **108**, 226101 (2012).
[24] R. Wittmann, C. E. Sitta, F. Smallenburg, and H. Löwen, J. Chem. Phys. **147**, 134908 (2017).
[25] J. M. Brader, R. Evans, and M. Schmidt, Mol. Phys. **101**, 3349 (2003).
[26] S. M. Cox and P. C. Matthews, J. Comput. Phys. **176**, 430 (2002).
[27] A. Adland, A. Karma, R. Spatschek, D. Buta, and M. Asta, Phys. Rev. B **87**, 024110 (2013).
[28] D. Stopper and R. Roth, J. Chem. Phys. **147**, 064508 (2017).
[29] J. Nickolls, I. Buck, M. Garland, and K. Skadron, ACM Queue **6**, 40 (2008).
[30] M. Oettel, J. Phys.: Condens. Matter **24**, 464124 (2012).
[31] H.-J. Butt, K. Graf, and M. Kappl, *Physics and Chemistry of Interfaces* (Wiley-VCH, Weinheim, 2003), Chap. 3.
[32] B. Carey, L. Scriven, and H. Davis, AIChE J. **26**, 705 (1980).
[33] J. G. Eberhart, J. Phys. Chem. **70**, 1183 (1966).
[34] R. L. Schmidt, J. C. Randall, and H. L. Clever, J. Phys. Chem. **70**, 3912 (1966).
[35] A. E. Gonzalez, Crystals **6**, 46 (2016).
[36] M. Amini and B. B. Laird, Phys. Rev. B **78**, 144112 (2008).
[37] C. A. Becker, D. L. Olmsted, M. Asta, J. J. Hoyt, and S. M. Foiles, Phys. Rev. B **79**, 054109 (2009).
[38] R. L. Vink, T. Neuhaus, and H. Löwen, J. Chem. Phys. **134**, 204907 (2011).